



Effects of smectite dehydration and illitisation on overpressures in sedimentary basins: A coupled chemical and thermo-hydro-mechanical modelling approach

Joachim Tremosa, Hélène Gailhanou, Christophe Chiaberge, Raymi Castilla, Eric Gaucher, Arnault Lassin, Claude Gout, Claire Fialips, Francis Claret

► To cite this version:

Joachim Tremosa, Hélène Gailhanou, Christophe Chiaberge, Raymi Castilla, Eric Gaucher, et al.. Effects of smectite dehydration and illitisation on overpressures in sedimentary basins: A coupled chemical and thermo-hydro-mechanical modelling approach. *Marine and Petroleum Geology*, 2020, 111, pp.166-178. 10.1016/j.marpetgeo.2019.08.021 . hal-02734936

HAL Id: hal-02734936

<https://brgm.hal.science/hal-02734936>

Submitted on 20 Jul 2022

HAL is a multi-disciplinary open access archive for the deposit and dissemination of scientific research documents, whether they are published or not. The documents may come from teaching and research institutions in France or abroad, or from public or private research centers.

L'archive ouverte pluridisciplinaire **HAL**, est destinée au dépôt et à la diffusion de documents scientifiques de niveau recherche, publiés ou non, émanant des établissements d'enseignement et de recherche français ou étrangers, des laboratoires publics ou privés.



Distributed under a Creative Commons Attribution - NonCommercial 4.0 International License

1 Effects of smectite dehydration and illitisation on overpressures in sedimentary
2 basins: a coupled chemical and thermo-hydro-mechanical modelling approach

3

4 Joachim Tremosa^{a,*}, Helene Gailhanou^a, Christophe Chiaberge^a, Raymi Castilla^b, Eric C. Gaucher^b,
5 Arnault Lassin^a, Claude Gout^b, Claire Fialips^b and Francis Claret^a

6

7 a BRGM, 3 av. Claude Guillemin, BP 36009, 45060 Orléans, France

8 b TOTAL S.A., Avenue Larribau, 64018 Pau, France

9

10 Corresponding author:

11 Joachim TREMOSA

12 BRGM, 3 av. Claude Guillemin BP6009

13 45060 Orléans, France.

14 * E-mail: j.tremosa@brgm.fr

15

16

17

18 **Abstract**
19 Diagenetic smectite dehydration and smectite-to-illite transition in clay-rich sediments can contribute
20 to the generation of overpressure in sedimentary basins, because of the release of water associated
21 with these mineralogical reactions. However, the challenge of deciphering the contribution of smectite
22 dehydration and illitisation to fluid pressure amongst other mechanisms generating overpressure
23 requires the different mechanisms at play to be jointly considered. Here, we developed a coupled
24 chemical and thermo-hydro-mechanical code, named SURP, to calculate the overpressure generation
25 in a sedimentary pile because of sediment compaction during its burial, temperature increase, water
26 flow and because of the release of water by clay dehydration and illitisation. For this purpose, a
27 revised thermodynamic model describing smectite dehydration by a solid solution approach was
28 considered, together with the different thermo-hydro-mechanical processes occurring in sedimentary
29 basins. The SURP code was applied to the case study of an overpressured passive margin in the Niger
30 Delta, composed of thick shale layers in a sedimentary pile. In this geological scenario, smectite
31 dehydration was simulated and could explain 10 to 30 % (20 to 50 bar) of the present day
32 overpressure in the main reservoirs, in addition to compaction disequilibrium.

33

34 **Keywords:** overpressure; smectite; dehydration; fluid generation; fluid pressure; THMC; Niger Delta

35

36

37 **1. Introduction**

38

39 Overpressures, or abnormal fluid pressures, are frequently encountered in sedimentary basins and
40 consist in fluid pressures exceeding the hydrostatic head. During the drilling of deep reservoirs, it is
41 necessary to anticipate and to be able to control the fluid pressure conditions for ensuring well
42 integrity and safety. Understanding the fluid pressure regime is also useful for evaluating fluid and
43 hydrocarbon migration and trapping over the sedimentary basin history. The water flushing of
44 hydrocarbons linked to overpressures can clearly be a cause of unsuccessful results during exploration
45 phases.

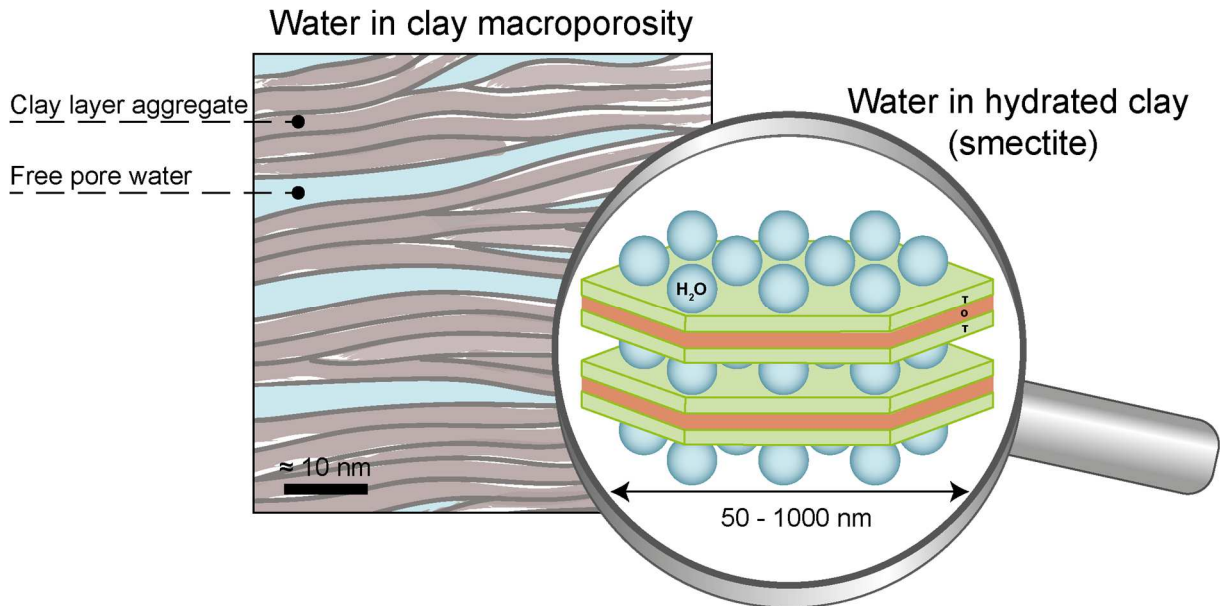
46 These overpressures generally correspond to a delay in the expulsion of the fluids contained in the
47 porosity and can be caused by different mechanisms (Neuzil, 1995; Swarbrick and Osborne, 1998),
48 including: i) mechanical compaction disequilibrium; ii) tectonic compression; iii) mineralogical
49 transformations releasing water; iv) hydrocarbon generation; or v) osmotic processes. Combinations of
50 several of these mechanisms are frequently the cause of the abnormal pressure profile in a sedimentary
51 pile and, for interpreting or predicting overpressure, it is necessary to distinguish the respective
52 contribution of each mechanism. For this purpose, the use of basin models able to calculate the
53 pressure evolution in the sedimentary pile by taking into account the different mechanisms generating
54 overpressures is a pertinent approach (Swarbrick and Osborne, 1998; Wangen, 2001; Nordgård Bolås
55 et al., 2004; Tremosa et al., 2012).

56 Overpressures linked to the presence of clay layers are not always correctly interpreted. We have to
57 distinguish (i) the water produced by mechanical compaction and from the macroporosity of the clay
58 formations and (ii) the water produced by the thermodynamic transformation of the clay minerals
59 (Figure 1). By thermodynamic transformation, we mean the dehydration of smectite and the illitisation
60 processes of hydrated smectite. Several cases of overpressures generated by clay dehydration are
61 reported in the literature (Bruce, 1984; Shaw and Primmer, 1989; Kooi, 1997; Gordon and Flemings,
62 1998; Nordgård Bolås et al., 2004; Tanikawa et al., 2008), as an additional mechanism to compaction
63 disequilibrium. However, clay dehydration is ruled out in most studies on the origin of overpressures

64 and is only considered as one unloading process amongst others that decreases the effective stress
65 without changing the porosity. Clay dehydration is rarely considered in forward modelling of
66 overpressure build-up but some models have done so, suggesting that clay dehydration can contribute
67 up to $\frac{1}{3}$ of the overpressure, depending on the geological scenario (Audet, 1995; Wangen, 2001).
68 When smectite dehydration and illitisation were considered in a pressure or transport calculation
69 model in a sedimentary basin (Audet, 1995; Wangen, 2001; Saffer and McKiernan, 2009), the
70 mineralogical process releasing water was simplified, only describing a continuous release of water
71 depending on temperature but without considering thermodynamic constraints and dehydration steps.
72 Conversely, when a thermodynamic model was established and used to correctly describe clay
73 dehydration, the coupling with the pressure calculation was partial (Colten-Bradley, 1987; Meiller,
74 2013). In these last models, the pressure corresponding to the volume of released water was added to
75 the calculated pressure, thus accounting for compaction but without considering the feedback of this
76 additional pressure excess on flow and effective stress.

77 In this paper, we are presenting a model, called SURP, for pore pressure calculation during the burial
78 of a sedimentary pile, accounting for water flow, compaction, temperature increase and involving an
79 advanced thermodynamic model describing smectite dehydration (Vidal and Dubacq, 2009). Hence,
80 pore pressure is calculated by considering both the different thermo-hydro-mechanical processes
81 occurring in a sedimentary basin and the release of water by smectite, calculated depending on the
82 modelled temperature and pressure evolution. A coupled approach considering a sound description of
83 clay dehydration in pore pressure calculation was missing to evaluate the influence of smectite
84 dehydration on overpressure generation. The developed model was applied to a case study in the Niger
85 Delta, where the influence of water released by thick shale layers on overpressure is discussed.

86



87

88 *Figure 1. Schematic view of the distribution of water in a clay-rock: in the macroporosity between clay aggregates and in the*
 89 *interlayer space between clay crystallite.*

90

91 **2. Model development for overpressure calculations during burial diagenesis of**
 92 **marine sediments**

93

94 **2.1. Objective of the SURP code**

95 The SURP code has been developed to account for both thermo-hydro-mechanical and mineralogical
 96 effects and their reciprocal influence, including the influence of temperature and pressure evolution on
 97 clay dehydration and the influence of the water released by mineralogical reactions on the flow, the
 98 fluid pressure and the effective stress in the sedimentary pile. In the SURP coupling approach, the
 99 thermo-hydro-mechanical calculations are made using a Python code source that can be coupled
 100 through a sequential non-iterative approach with the IPHREEQC geochemical calculation code

101 (Charlton and Parkhurst, 2011) used to carry out the thermodynamic and mineralogical calculations.

102 Hence, the aim of the SURP code is to evaluate the effect of water releases by smectite mineralogical
 103 transformations on the pore pressure in a sedimentary pile and in particular in clayey layers. The
 104 geological context of application corresponds to a passive margin in the marine domain, where the
 105 clay layer of interest is buried over time because of the deposition of overlying sediments. The
 106 principle of the pore pressure calculation consists in considering the following processes in a 1D
 107 sedimentary pile over time:

- 108 • Sediment deposition;
- 109 • Burial and compaction due to overlying sediments giving rise to a porosity reduction and a
- 110 decrease of the sediment thickness;
- 111 • Temperature increase with depth;
- 112 • Water release during clay mineral transformations;
- 113 • Modification of the thermal, hydraulic and mechanical properties of the rock during the burial;
- 114 • Water flow in the sedimentary pile and possible overpressure build-up.

115

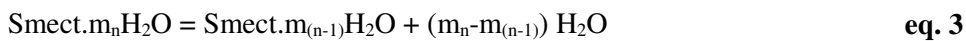
116 **2.2. Thermodynamic model for dehydration of smectites**

117 A thermodynamic model was implemented in the SURP code in order to assess the amount of water
 118 released by the dehydration of smectites occurring during the burial of sediments. The proposed
 119 thermodynamic approach, based on solid solution models, aims to describe the thermodynamic
 120 properties of the smectite mineral as well as the amount of hydration water bound to the smectite, i.e.
 121 interlayer water, as a function of temperature, pressure and water activity. It was adapted from the
 122 model from Vidal and Dubacq (2009) established to simulate the dehydration of dioctahedral Al-
 123 smectites and the smectite-to-illite conversion occurring with increasing temperature and pressure and
 124 decreasing water activity.

125 2.2.1. Dehydration model from Vidal and Dubacq (2009)

126 According to the Vidal and Dubacq (2009) model, the compositional and interlayer charge variations
 127 of dioctahedral smectite and illite can be described by non-ideal solid solutions using three end-
 128 members, namely hydrated beidellite ($\text{Beid} \cdot m_n\text{H}_2\text{O}$) $\text{R}^{+0.3}[\text{Al}_2]^{VI}[\text{Al}_{0.3}\text{Si}_{3.7}]^{IV}\text{O}_{10}(\text{OH})_2, m_n\text{H}_2\text{O}$,
 129 dehydrated beidellite (Beid.A) $\text{R}^{+0.3}[\text{Al}_2]^{VI}[\text{Al}_{0.3}\text{Si}_{3.7}]^{IV}\text{O}_{10}(\text{OH})_2$, and anhydrous R⁺-mica
 130 ($\text{R}^{+}[\text{Al}_2]^{VI}[\text{AlSi}_3]^{IV}\text{O}_{10}(\text{OH})_2$, with $\text{R}^{+} = \text{K}^{+}, \text{Na}^{+}, 0.5\text{Ca}^{2+}$, or 0.5Mg^{2+}). Four solid solutions were
 131 defined, with four hydrated beidellite end-members at $m_0 = 0.7$, $m_1 = 2$, $m_2 = 4$ and $m_3 = 7$
 132 $\text{H}_2\text{O}/\text{O}_{10}(\text{OH})_2$, for the beidellite end-members at 0, 1, 2 and 3 water layers, respectively. Besides, the
 133 amounts of interlayer water in the hydrated beidellite end-members were assumed not to depend on the
 134 nature of the interlayer cation. Therefore, considering a dioctahedral smectite with an intermediary

135 composition between beidellite and R⁺-mica , the Vidal and Dubacq (2009) model can predict the most
136 stable solid solution amongst the four solid solutions Beid.A-Beid. m_n H₂O-Mica, at fixed pressure,
137 temperature and water activity. The transition between smectite with n and ($n-1$) layers occurs at fixed
138 temperature and water activity, with the simultaneous attainment of the following equilibria:



139 Such a transition generates a sudden release of water, calculated from the conditions of equilibrium
140 (eq. 1 to 3). It results in a stepwise dehydration of smectite at each transition temperature. Besides,
141 inside the stability domain of a given solid solution, the variations of volume and water amount are
142 continuous, as described by the thermodynamic parameters of the non-ideal solid solution.

143 In our approach, the model from Vidal and Dubacq (2009) was not directly applicable for two main
144 reasons: (i) it is currently non-feasible to introduce non-ideal parameters for ternary solid solutions in
145 the IPHREEQC code (Charlton and Parkhurst, 2011) used for geochemical calculations in the SURP
146 code, and (ii) the compositional range of dioctahedral smectite is restricted to Si⁴⁺, Al³⁺ and interlayer
147 R⁺ (K⁺, Na⁺, Ca²⁺/2 or Mg²⁺/2) cations. Despite the model having been extended to (Al, Mg, Fe)
148 octahedral compositions of dioctahedral smectites by Dubacq et al. (2010), it required the use of non-
149 ideal quaternary solid solutions, not compatible with the IPHREEQC code. Nevertheless, we adapted
150 the model from Vidal and Dubacq (2009), by applying a similar methodology based on the use of solid
151 solutions with hydrated smectite end-members and dehydrated smectite, but restricted to binary solid
152 solutions and to a fixed smectite composition, assumed to be representative of the studied geological
153 system.

154

155 2.2.2. The smectite dehydration model in the SURP code

156 In the present approach, we consider a montmorillonite composition for smectite instead of a beidellite
157 composition because in natural diagenetic environments, the smectitic components in interstratified

158 illite-smectite are mostly reported to be of the montmorillonite type (Velde and Brusewitz, 1986;
159 Meunier and Velde, 1989; Srodon et al., 2009). Illite-beidellite mixed layers are less frequently
160 observed and generally associated with hydrothermal conditions.

161 The montmorillonite composition departs from the compositional ranges used in the Vidal and Dubacq
162 (2009) model, by its charge deficit located in the octahedral layer instead of the tetrahedral layer, due
163 to the concomitant presence of Al and Mg in octahedral sites. However, the approach used by the
164 authors for extracting the amounts of interlayer water and the energies of hydration as a function of the
165 water activity was based on experimental data obtained for montmorillonites, with interlayer charges
166 at $\sim 0.35 - 0.38$ eq/O_{10(OH)₂} (Ferrage et al., 2005). For this reason, the hydration parameters were
167 similar to those used in the Vidal and Dubacq (2009) model for hydrated beidellite end-members.
168 Finally, our model was using three binary solid solutions between the hydrated montmorillonite end-
169 member and the dehydrated end-member. The hydrated components, Mnt_Na.3w (3 water layers),
170 Mnt_Na.2w (2 water layers) and Mnt_Na.1w (1 water layer), contain respectively $m_3 = 7$, $m_2 = 4$ and
171 $m_1 = 2 \text{ H}_2\text{O}/\text{O}_{10(\text{OH})_2}$.

172 The thermodynamic properties of the dehydrated montmorillonite (ΔH_f° , S° , V_m° , $C_p(T)$) were
173 estimated using the set of predicting models from Blanc et al. (2015). These models for enthalpy,
174 entropy, molar volume and heat capacity function were all calibrated using a common and consistent
175 thermodynamic dataset, based on a rigorous selection between experimental data from the literature
176 and associated exclusively with phyllosilicates. This recent work provides a consistent dataset for
177 smectites and was thus preferred to the approach used by Vidal and Dubacq (2009), which combined
178 different methods for enthalpy, entropy and heat capacity function.

179 Estimation of the thermodynamic dataset for the hydrated end-members was performed according to
180 the procedure described by Vidal and Dubacq (2009), except for molar volumes. The thermodynamic
181 parameters ($\Delta H_f^\circ m_n \text{H}_2\text{O}$, $S^\circ \text{H}_2\text{O}_{(i)}$, $C_p(T)$) associated with interlayer water for Na-montmorillonite end-
182 members are the same as those used by Vidal and Dubacq (2009) for Na-beidellite end-members
183 (Table 1). The molar volumes V_m° of hydrated montmorillonites at n water layers ($n = 1, 2, 3$) were
184 estimated using the recent advances from Meiller (2013). The author established functions to express

185 the dependency of the molar volume on the number of water layers, the nature of the interlayer cation
186 (Na and Ca) and the substitution rate Al-Mg in the octahedral sites of the smectite.

187 The non-ideality of the solid solutions is described by the same Margules parameters as those used in
188 the Vidal and Dubacq (2009) model, extracted from the Ransom and Helgeson (1994) model. Their
189 values were assumed at $W = -10$ kJ for Smect. m_n H₂O – Smect.A ($n = 1, 2$ or 3 water layers) in the case
190 of dioctahedral smectites.

191 Finally, the thermodynamic dataset used for the solid-solution models is reported in Table 1 and Table
192 2, in the case of the low-charge montmorillonite Na_{0.33}Si₄(Al_{1.67}Mg_{0.33})O₁₀(OH)₂ (Mnt_Na).

193

194 *Table 1. Standard-state thermodynamic properties of the montmorillonite end-members.*

	$m_n\text{H}_2\text{O}$ (mol/O ₁₀ (OH) ₂)	ΔG_f° (kJ/mol)	ΔH_f° (kJ/mol)	S° (J/mol/K)	V° (cm ³ /mol)	A	B	C	$\Delta H_f^\circ m_n\text{H}_2\text{O}$ (kJ)
Mnt_Na.A	0	-5320.51*	- 5688.74*	276.76*	133.83*	330.7*	225.94*	-78.055*	
Mnt_Na.1w	2	-5806.02	-6280.54	386.76	170.53	419.37	275.26	-91.74	293.85
Mnt_Na.2w	4	-6283.23	-6864.04	496.76	207.13	508.05	324.58	-105.43	291.75
Mnt_Na.3w	7	-6994.77	-7735.03	661.76	258.63	641.06	398.56	-125.96	290.33

Notes: The $C_p(T)$ functions of the clay minerals are expressed by $C_p(T) = A + 10^{-3} B T + 10^5 C T^2$, where A , B and C are Maier-Kelley coefficients.

(*) estimated from Blanc et al. (2015) model

The properties of interlayer water, $\Delta H_f^\circ m_n\text{H}_2\text{O} = (H_f^\circ \text{Mnt.}m_n\text{H}_2\text{O} - H_f^\circ \text{Mnt.}m_{(n-1)}\text{H}_2\text{O})/(m_n - m_{(n-1)})$, $C_p(T)$ function and entropy $S^\circ \text{H}_2\text{O}_{(i)} = 55$ J/mol/K are given by Vidal and Dubacq (2009).

The molar volumes of hydrated end-members are calculated according to Meiller (2013).

195

196

197

198

199

200 *Table 2. Temperature dependency of the equilibrium constant for the reaction of dissolution of the montmorillonite end-members.*

	$\log K$	A_1	A_2	A_3	A_4	A_5	Reaction of dissolution
Mnt_Na.A	3.31	-1.1860978E+03	-2.0559084E-01	6.2330921E+04	4.3249803E+02	-2.5368937E+06	$\text{Na}_{0.33}\text{Mg}_{0.33}\text{Al}_{1.67}\text{Si}_4\text{O}_{10}(\text{OH})_2 + 6\text{H}^+ + 4\text{H}_2\text{O} = 1.67\text{Al}^{+++}$ + 0.33Mg ⁺⁺ + 0.33Na ⁺ + 4H ₄ SiO ₄
Mnt_Na.1w	1.35	-1.1353999E+03	-1.9610007E-01	5.8199874E+04	4.1458388E+02	-2.2979605E+06	$\text{Na}_{0.33}\text{Mg}_{0.33}\text{Al}_{1.67}\text{Si}_4\text{O}_{10}(\text{OH})_2 \cdot 2\text{H}_2\text{O} + 6\text{H}^+ + 2\text{H}_2\text{O} = 1.67\text{Al}^{+++} + 0.33\text{Mg}^{++} + 0.33\text{Na}^+ + 4\text{H}_4\text{SiO}_4$
Mnt_Na.2w	0.83	-1.0826594E+03	-1.8627762E-01	5.4396671E+04	3.9592168E+02	-2.0533067E+06	$\text{Na}_{0.33}\text{Mg}_{0.33}\text{Al}_{1.67}\text{Si}_4\text{O}_{10}(\text{OH})_2 \cdot 4\text{H}_2\text{O} + 6\text{H}^+ = 1.67\text{Al}^{+++} + 0.33\text{Mg}^{++} + 0.33\text{Na}^+ + 4\text{H}_4\text{SiO}_4$
Mnt_Na.3w	0.81	-1.0149545E+03	-1.7339608E-01	4.9505162E+04	3.7210547E+02	-1.7182698E+06	$\text{Na}_{0.33}\text{Mg}_{0.33}\text{Al}_{1.67}\text{Si}_4\text{O}_{10}(\text{OH})_2 \cdot 7\text{H}_2\text{O} + 6\text{H}^+ = 1.67\text{Al}^{+++} + 0.33\text{Mg}^{++} + 0.33\text{Na}^+ + 4\text{H}_4\text{SiO}_4 + 3\text{H}_2\text{O}$

Note: $\log K = A_1 + A_2 T + A_3/T + A_4 * \log(T) + A_5/T^2$

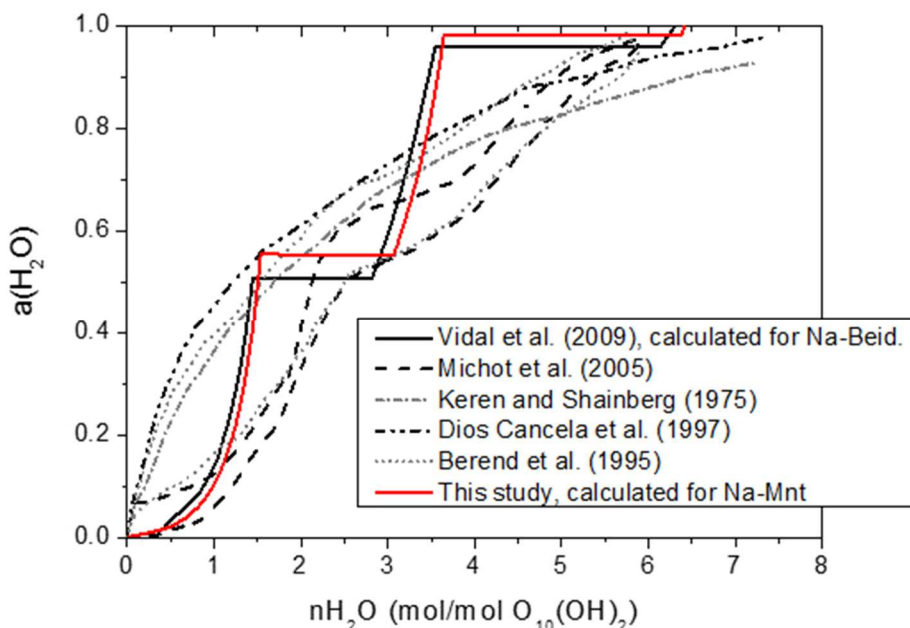
$\log K$ and A₁-A₅ parameters were calculated using the thermodynamic properties of aqueous species selected from the Thermoddem database (Blanc et al., 2012).

202

203 2.2.3. Verification of the consistency of the thermodynamic data for dehydrated and hydrated
204 Na-Montmorillonite

205 The consistency of the thermodynamic data for the dehydrated and hydrated Mnt_Na end-members
206 was first assessed by calculating the dehydration isotherm of the smectite at 25 °C and 1 bar pressure,
207 using PHREEQC v3 (Parkhurst and Appelo, 2013) and the Thermoddem database (Blanc et al., 2012)
208 (Figure 1).

209 The comparison with the stepwise dehydration isotherm is very consistent with the previous results
210 obtained by Vidal and Dubacq (2009) for Na-beidellite (Figure 2). These results are in reasonable
211 agreement with the experimentally determined basal spacing (not shown here) and hydration
212 isotherms, despite some differences due to the coexistence of smectites with different hydration states
213 in the experimental isotherms, as discussed in Vidal and Dubacq (2009).

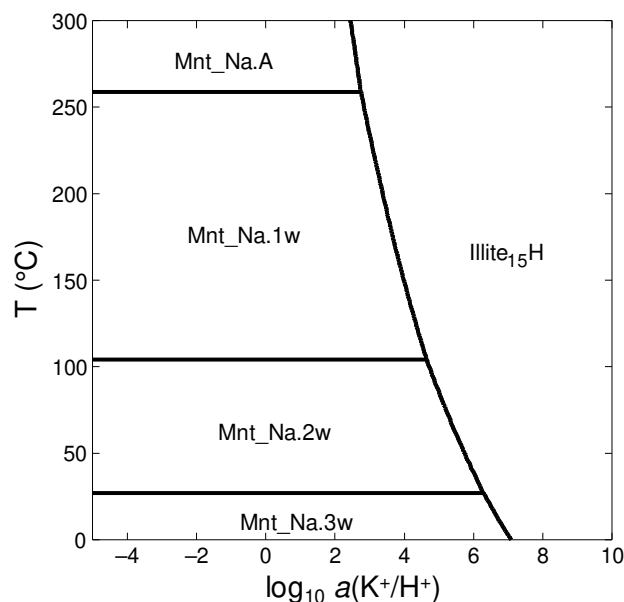


215 Figure 2. Comparison of measured dehydration isotherms for smectite with results from the Vidal and Dubacq (2009) model
216 and its adaptation for the Na-Montmorillonite.

217

218 A second verification was performed by calculating a phase diagram for the Na₂O-K₂O-SiO₂-Al₂O₃-
219 MgO-H₂O system (Figure 3), using the Geochemist's Workbench® software, at the saturation vapour

220 pressure. The results indicated that all smectite end-members (Mnt_Na.A, 1w, 2w, 3w) exhibit a
 221 stability domain depending on the temperature region, in which the corresponding solid solution is
 222 predominant. Moreover, the transition temperatures between the stability domains of the smectite end-
 223 members are consistent with those previously calculated by Vidal and Dubacq (2009) for Na-
 224 beidellite. This figure also highlights the expected behaviour of illite, the stability domain of which
 225 develops as the potassium concentration increases, and further enlarges at elevated temperatures.



226

227 *Figure 3. Composition-temperature phase diagram calculated for the Na₂O-K₂O-SiO₂-Al₂O₃-MgO-H₂O system*
 228 *(Illite₁₅H = K_{0.85}Si_{3.7}Al_{0.3}(Al_{1.85}Mg_{0.15})O₁₀(OH)₂). The activities of Na, H₄SiO₄, Al and Mg in solution are constrained by*
 229 *equilibrium reactions with minerals analcime, quartz, kaolinite and antigorite, respectively.*

230

231 2.2.4. Stability domains of solid solutions as a function of temperature and pressure

232 In order to take into account the effect of pressure on the stability domains of the solid solutions, the
 233 variation of the transition temperatures for the smectite end-members with pressure were calculated
 234 using the PHREEQC code. In the case of the montmorillonite Mnt_Na, the dependency of the
 235 transition temperatures on pressure is low and may be described by using linear functions (Table 3).

236 *Table 3. Limits of the stability domains as a function of temperature and pressure.*

Transition	Linear function
SS3w – SS2w	$P_{tr} = 115.84*T_{tr} - 3304.9$ ($R^2 = 0.9716$)
SS2w – SS1w	$P_{tr} = -67.021*T_{tr} + 6941$ ($R^2 = 0.9955$)

Notes: P expressed in bar, T in °C.

[SSnw means the solid solution Mnt_Na.nw-Mnt_Na.A]

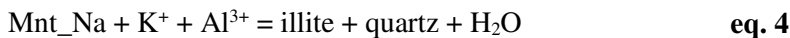
237

238 **2.3. Smectite-to-illite conversion model**

239 Smectite illitisation is widely described in the literature, notably in the case of burial diagenesis of
 240 clay-rich sediments (Weaver, 1959; Burst, 1969; Perry and Hower, 1970; Altaner and Ylagan, 1997;
 241 Lanson et al., 2009). The transformation process generates the formation of intermediate I/S phases,
 242 with illite content progressively increasing with temperature, the concentration of potassium in pore
 243 water, the water/rock ratio and geological time (Altaner and Ylagan, 1997). In the early stage of burial
 244 diagenesis, discrete smectite and randomly interstratified I/S coexist, with a progressive increase in
 245 illite content in the I/S. When the latter is higher than ~ 50% of illite (Inoue et al., 1987), short-range
 246 ordered (R1) interstratified I/S are observed. Lanson et al. (2009) showed notably from structural
 247 characterization of Texas Gulf Coast interstratified series that intermediate I/S phases and I/S/Chlorite
 248 phases may coexist. For the most illite-rich contents (> 85% illite), long-range ordered interstratified
 249 I/S ($R \geq 3$) are observed (Inoue et al., 1987).

250 Several kinetic models have been developed in order to describe the smectite-to-illite transformations
 251 during burial diagenesis in sedimentary basins (Altaner, 1989; Pytte and Reynolds, 1989; Velde and
 252 Vasseur, 1992; Cuadros, 2006). Among these models, that of Cuadros (2006) takes better account of
 253 the question of the availability of potassium for the smectite-to-illite reaction. Indeed, K concentration
 254 is the most problematic variable in the modelling of smectite illitisation kinetics, since it is affected by
 255 the competition with other exchangeable cations, also dependent on the degree of hydration of the
 256 smectite interlayers. The model from Cuadros (2006) involves the “effective K concentration”
 257 variable, which differs from the actual K concentration by integrating notably cationic exchange in
 258 smectitic interlayers.

259 Such a kinetic model cannot be easily implemented in our modelling approach based on water/rock
260 thermodynamic equilibrium considerations since it would require the thermodynamic parameters
261 associated with discrete I/S series to be determined and the dehydration of smectite layers with burial
262 depth to be taken into account. Finally, for the sake of simplicity, it is assumed that the smectite-to-
263 illite conversion does not involve the formation of interstratified I/S and can be roughly described by
264 the simplified reaction:



265 This equation is not balanced but simply aims to indicate that the smectite-to-illite transformation as
266 described in our model requires a source of potassium and aluminium and generates quartz. This
267 approach is consistent with the implementation of the dehydration model for montmorillonite Mnt_Na.

268

269 **2.4. Thermo-hydro-mechanical model including chemical forcing**

270 2.4.1. Water flow model

271 The pore pressure evolution in a porous media is calculated using the continuity equation which
272 describes the mass conservation in a given volume. Its general expression giving the variation over
273 time of the mass of water in a volume of saturated poroelastic media, accounting for a source term, is
274 expressed by (De Marsily, 1986; Ingebritsen et al., 2006):

$$\frac{\partial(n \rho_f)}{\partial t} = \nabla \left[\frac{k \rho_f}{\mu_f} (\nabla P - \rho_f g \nabla z) \right] + \Gamma \quad \text{eq. 5}$$

275 where, n is the porosity, ρ_f is the fluid density (kg.m^{-3}), k is the intrinsic permeability (m^2), μ_f is the
276 fluid dynamic viscosity (Pa.s), P is the pore pressure (Pa), g is the acceleration constant due to gravity
277 (9.81 m.s^{-2}), ∇z is $(0,0,1)$ if the z axis is orientated downward and Γ is a source term corresponding to the
278 input or withdrawal of water in the porosity. In the present case, this source term corresponds to the
279 water released by smectite dehydration and by smectite transformation to illite.

280 The continuity equation can be written in such a way that the variation of fluid mass can be dependent
281 on the variations over time of pore pressure, mechanical stress and temperature. This expression of
282 thermo-hydro-mechanical coupling including a vertical load stress which can vary over time can be
283 written as follows (Ingebritsen et al., 2006):

$$Ss' \frac{\partial P}{\partial t} - Ss' \xi \frac{d\sigma_{zz}}{dt} - \rho_f g \Lambda' \frac{\partial T}{\partial t} = \nabla \left[g \frac{k \rho_f}{\mu_f} (\nabla P - \rho_f g \nabla z) \right] + \Gamma \quad \text{eq. 6}$$

284 In this expression, Ss' is the unidimensional specific storage coefficient (m^{-1}), ξ is an unidimensional
 285 loading coefficient (dimensionless), σ_{zz} is the total vertical stress (Pa), Λ' is the thermal response
 286 coefficient ($^{\circ}\text{C}^{-1}$) and T is the temperature ($^{\circ}\text{C}$).
 287 The unidimensional specific storage coefficient is expressed by (Van Der Kamp and Gale, 1983):

$$Ss' = \rho_f g [(c_b - c_s)(1 - \lambda) + (nc_f - nc_s)] \quad \text{eq. 7}$$

288 The unidimensional loading coefficient is defined as:

$$\xi = \frac{B(1 + \nu)}{3(1 - \nu) - 2\alpha B(1 - 2\nu)} \quad \text{eq. 8}$$

289 with:

$$\lambda = \frac{2\alpha(1 - 2\nu)}{3(1 - \nu)} \quad \text{eq. 9}$$

290 where, c_f , c_b and c_s , are the compressibilities (Pa^{-1}) of fluid, porous media and solid, respectively, B is
 291 the Skempton coefficient (dimensionless), ν the Poisson's ratio (dimensionless) and α is the Biot
 292 coefficient (dimensionless).

293 Skempton and Biot coefficients can be expressed as a function of the compressibilities of fluid, porous
 294 media and solid. Thus:

$$B = \frac{c_b - c_s}{(c_b - c_s) + n(c_f - c_s)} \quad \text{eq. 10}$$

295 and:

$$\alpha = 1 - \frac{c_s}{c_b} \quad \text{eq. 11}$$

296 The compressibilities of fluid, porous media and solid can be expressed as a function of the Young
 297 modulus E (Pa), a parameter dependent on the material:

$$c_b = \frac{3(1 - 2\nu)}{E} \quad \text{eq. 12}$$

$$c_s = \frac{(1 - 2\nu)(1 + \nu)}{E(1 - \nu)} \quad \text{eq. 13}$$

298 To solve the flow equation (**eq. 6**), it is then necessary to determine the different coefficients involved,
 299 which can be written as a function of properties of the fluid, the solid and the porous media
 300 (Supplementary material A). It is also necessary to calculate the variation over time of the mechanical
 301 stress and of the temperature in the considered volume. The vertical mechanical stress is calculated
 302 from the weight of the sediments overlying the considered point, as follows:

$$\sigma_{zz} = \int_0^z \rho_b g dz \quad \text{eq. 14}$$

303 where, ρ_b is the porous media density, obtained from the porosity and the fluid and solid densities:
 304 $\rho_b = \rho_s(1 - n) + \rho_f n$; or directly from a density well log.
 305 Temperature is obtained from the depth and the geothermal gradient (G_T in $^{\circ}\text{C.m}^{-1}$). Hence, sediment
 306 temperature increases over time with sediment burial. Temperature is calculated as follows:

$$T = G_T z \quad \text{eq. 15}$$

307 The source term for the input or withdrawal of water Γ ($\text{kg.m}^{-3}.\text{s}^{-1}$) in the continuity equation (**eq. 6**)
 308 corresponds to a mass of water produced or extracted in the porosity for a given volume and for a
 309 given length of time. Since the thermo-hydro-mechanical calculation is made for a 1D geometry, there
 310 is no notion of volume. The mass of water liberated or consumed by mineralogical reactions and
 311 calculated using IPHREEQC for 1kg of water (by convention) is then converted to m^3 of porous
 312 media, in order to respect the mass balance in the pressure calculation. The balance of the water
 313 released and consumed by mineralogical reactions that needs to be respected between Python and
 314 IPHREEQC can thus be written as follows:

$$\Gamma = \frac{d}{dt}(\text{solution_volume}) \times \rho_f \times n \quad \text{eq. 16}$$

315 where, dt is the time step length (s). The solution density ρ_f is calculated by IPHREEQC depending
 316 on its chemical composition and the temperature and pressure conditions.

317

318 2.4.2. Compaction model

319 During their burial in a sedimentary basin, sediments experience compaction because of the deposition
 320 of overlying sediments. Compaction is a deformation mechanism which gives rise to a reduction of the

321 porosity. In a basin model, this reduction of porosity is calculated using relationships introducing a
 322 dependence on the depth (e.g. Athy's law) or using relationships calculating the porosity as a function
 323 of the effective stress undergone by the rock. The latter kind of expressions allows the driving
 324 mechanism of porosity reduction, i.e., the effective stress, to be taken into account. One of these
 325 expressions which was shown to provide interesting results (Lambe and Whitman, 1979; Burland,
 326 1990; Nygård et al., 2004) is used in the present work:

$$e = e_0 - C_c \log \left(\frac{\sigma_{zz}'}{\sigma_{zz0}'} \right) \quad \text{eq. 17}$$

327 where, e is the void ratio (dimensionless), linked to porosity by the relation $e = n/(1 - n)$, C_c is the
 328 compaction index (dimensionless) and σ_{zz}' is the vertical effective stress (Pa). e_0 is the void ratio for
 329 the reference value of vertical effective stress σ_{zz0}' . This reference value corresponds to the
 330 consolidation limit of the rock and is considered equal to 1 MPa in the calculations. The rock has an
 331 elastic behaviour for effective stress lower than this limit and has a plastic behaviour for effective
 332 stress values higher than this consolidation limit. In this case the deformation undergone by the rock is
 333 irreversible. This porosity model dependent on the effective stress can be used in the present
 334 calculations because the weight of the sediments and the pore pressure are known.

335 As a consequence of the compaction of the rock and of the associated porosity reduction, the thickness
 336 of each lithological level and of each cell in the numerical model diminishes. The collapse of the cells
 337 is considered to be instantaneous (no time effect on deformation such as creep or stress relaxation) and
 338 the hypothesis is made that the solid is incompressible. The thickness diminution is thus only
 339 dependent on the loss of porosity. The new cell thickness is calculated by the balance between the
 340 initial thickness and porosity and the new porosity after compaction.

341 The effective stress necessary to calculate the porosity reduction by compaction (eq. 17) is calculated
 342 as follows:

$$\sigma'_{zz} = \sigma_{zz} - \alpha P \quad \text{eq. 18}$$

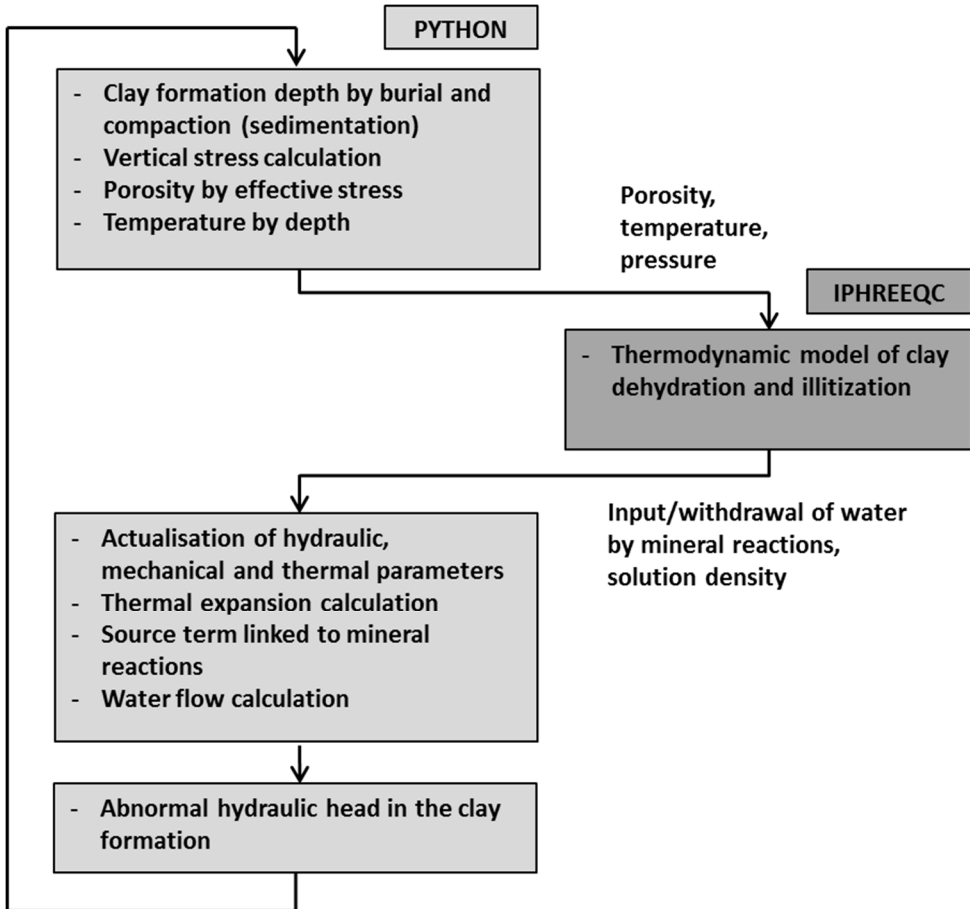
343 Biot's equation is preferred to Terzaghi's original equation to calculate the effective stress because it
 344 has been shown that using a Biot coefficient of 1 (or no Biot coefficient) gives overestimated porosity

345 reductions in overpressured areas (Burrus, 1998). In addition, the Biot coefficient actually varies with
346 porosity and becomes lower than 1 when porosity decreases (Supplementary material A).

347

348 **2.5. IPHREEQC-Python coupling**

349 One of the main goals of the SURP code is to jointly consider thermo-hydro-mechanical evolution and
350 mineralogical transformations in the geological system under study. Hence, calculation of the
351 chemical reactions has to consider the thermo-hydro-mechanical evolution of the system and,
352 inversely, thermo-hydro-mechanical calculation needs to take into account the effect of the chemical
353 reactions. In this way, a sequential non-iterative approach has been implemented whereby the thermo-
354 hydro-mechanical model is solved numerically using Python v 2.7 language and the chemical and
355 mineralogical reactions are calculated with IPHREEQC. At each time step, the reactive calculations
356 using IPHREEQC are launched from Python as a DLL dynamic library, using updated parameters as a
357 function of pressure, temperature and porosity evolution on the sedimentary pile. Once the
358 IPHREEQC calculations have been made, the mineralogical evolution, the balance of water produced
359 and consumed by the minerals and the solution density are entered into the thermo-hydro-mechanical
360 calculations in Python. The architecture of these coupled calculations is schematised in Figure 4,
361 where the successive calculations and parameters updating during one time-step are shown. Each time
362 step gives rise to the numerical resolution of the pore pressure in the sedimentary sequence and allows
363 the resulting overpressure to be calculated.



364

365 *Figure 4. Architecture of the calculations made during one time step by the SURP code, including the coupling of the thermo-*
366 *hydro-mechanical calculations with Python language and the thermodynamic reactive calculations made using the*
367 *IPHREEQC code.*

368

3. Effect of clay mineralogical reactions on overpressures in Niger Delta

In order to evaluate the influence of smectite dehydration and illitisation effects on overpressure, the SURP code was applied to a pore pressure calculation in the case of the Niger Delta. An overpressure has been reported in this area, which is formed of thick shale layers and where the geothermal gradient is normal. It appeared preferable to apply the SURP code to a real geological context than to limit its application to generic scenarii because the pore pressure that can be calculated with such a model is highly dependent on the sedimentary pile geometry, the sedimentation rate or the temperature evolution (Audet, 1995; Wangen, 2001).

3.1. Geological context of the Niger Delta

378 In the Niger Delta, the Akata, Agbada and Benin formations have been successively depositing since
379 the Tertiary during various prograding megasequences in the Gulf of Guinea (Whiteman, 1982;

380 Chukwu, 1991). The Akata formation is the basis of deltaic deposits and is formed of thick clay
381 deposits (up to 7000 m thick) which act as the primary source of hydrocarbons in the Niger Delta. The
382 Agbada formation has been depositing since the Eocene and presents alternations of claystone and
383 sandstone layers over 4000 m thick. Most of the hydrocarbon reservoirs are located in the Agbada
384 formation. The Benin formation is the youngest one and is formed of alluvial and shoreline sand
385 deposits.

386 The Niger Delta was identified for a long time as being an area presenting overpressures in particular
387 in the deepest parts (Akata Fm). By applying the equivalent depth method on onshore and offshore
388 wells of the Niger Delta, Owolabi et al. (1990) estimated that compaction disequilibrium is the main
389 cause of overpressures. By using 3D seismic data velocities, Opara (2011) showed that overpressures
390 are frequent, in particular in the deepest layers (up to 10 km deep). In these layers, a relationship has
391 been observed between overpressured zones and the presence of shale diapirs and slippage structures.
392 Ugwu and Nwankwo (2014) also reported overpressures linked to shale diapirism. According to
393 Cobbold et al. (2009), overpressures are effectively linked to compression structures but the main
394 cause of overpressures in Akata Fm and at the base of the Agbada Fm is due to hydrocarbon
395 generation associated with chemical compaction. In this mechanism, hydrocarbon generation reaches
396 the rock failure pressure, and the rupture of the cohesive grains associated with the weight of overlying
397 sediments gives rise to a more efficient recompaction of the rock, which is lithified again by
398 diagenesis. Multiple causes were also proposed by Caillet and Batiot (2003), Nordgård Bolås et al.
399 (2004) or Nwozor et al. (2013) to explain the overpressures in the Niger Delta, based on the
400 observation that compaction disequilibrium is not enough to reproduce the measured pressure profile.
401 Besides, Meiller (2013) showed that the mechanism of smectite dehydration can contribute
402 significantly to the generation of overpressures in the Niger Delta.

403 Several studies report mineralogical analyses at different depths across the Niger Delta sedimentary
404 pile (Braide and Huff, 1986; Odigi, 1986; Oboh, 1992; Jubril et al., 1998), showing both a
405 transformation of smectite to interstratified illite/smectite and to illite over depth. These studies show
406 that illitisation progress is mainly limited by potassium availability and its mobility. Potassium is
407 initially available from the seawater filling the pores as sediments are deposited and from the K-

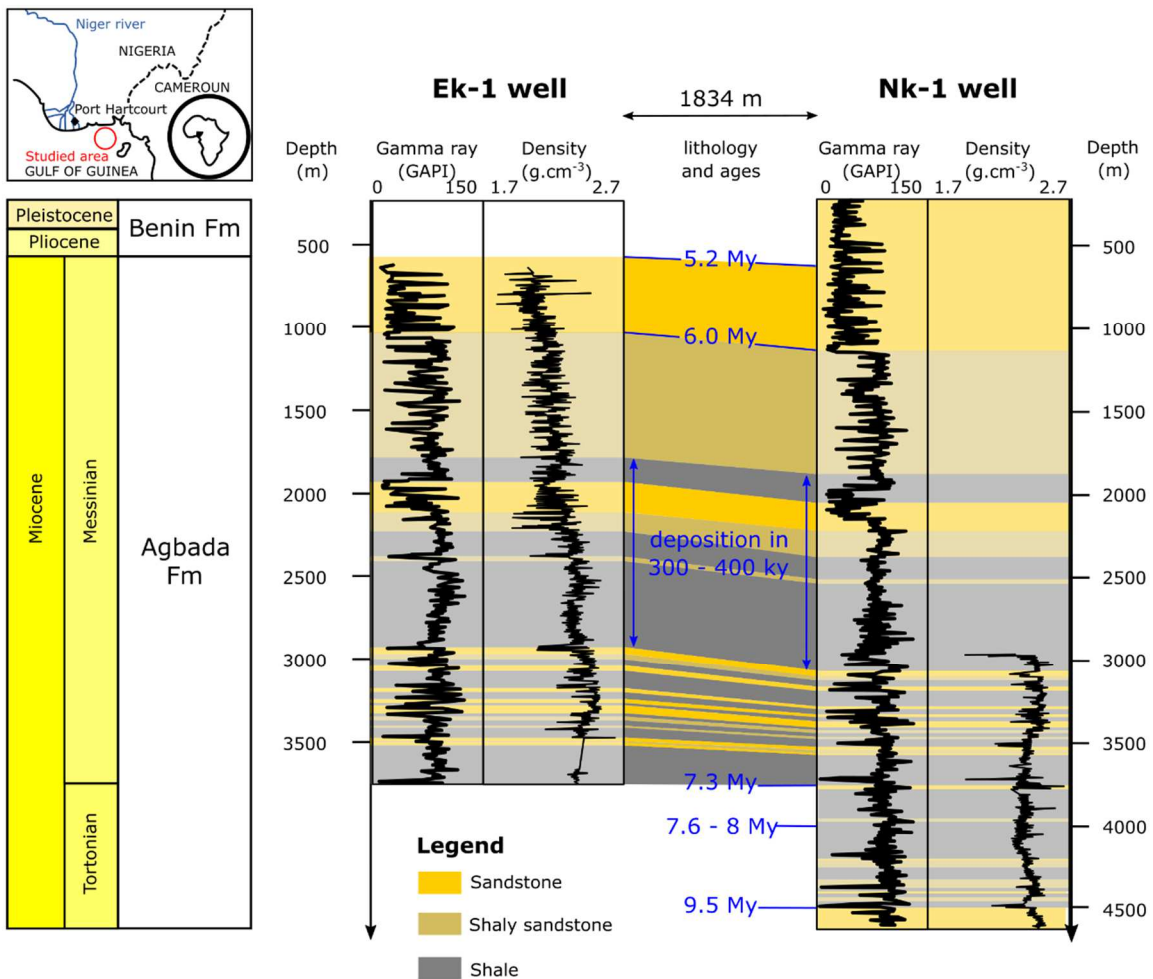
408 bearing minerals (feldspars, micas). Then, carbonate cementation and overpressures are controlling
409 potassium mobility in the sedimentary pile.

410 **3.2. Well data from the studied area**

411 The studied area (Figure 5) is located in the East of the Niger Delta (Nigeria) in shallow marine areas
412 (seabed at about 20 m deep). Data were obtained from different exploration wells and mainly from the
413 Ek-1 and Nk-1 wells that reach depths of 3750 and 4640 m, respectively. Benin Fm from the Pliocene
414 to the present day is found over the first 1100 meters. Wells then reach the Agbada Fm of Tortonian
415 and Messinian ages. Lithologies found are poorly consolidated sand with rare clay layers in the Benin
416 Fm. The upper part of the Agbada Fm presents alternations of shales and sandstones. Deeper, these
417 alternations are dominated by claystones whose layers can reach a thickness of several hundreds of
418 meters. Shales from the deeper Akata Fm are not reached by the wells.

419 Several logs (gamma ray, resistivity, sonic, neutron density) of Ek-1 and Nk-1 wells describe the
420 lithology and parameters such as the porosity and the apparent density as a function of depth (Figure
421 5). The correlated stratigraphic surfaces of the two wells were dated, based on regional
422 biostratigraphic markers. These datings indicate a variation of the sedimentation rate over time, with a
423 thickness of 3500 to 4000 m of Agbada Fm deposited over 3.5 My while a 500 to 1000 m-thickness of
424 the superficial Benin Fm was deposited over 5.2 My.

425



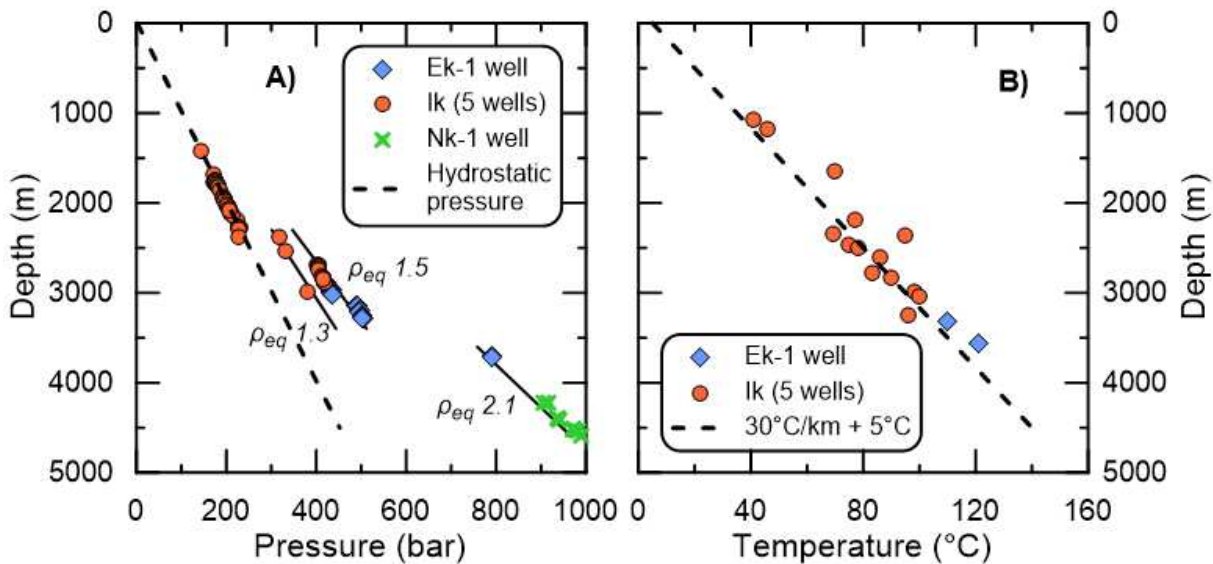
426

427 *Figure 5. Interpreted log of Ek-1 and Nk-1 wells with a correlation and dating of the major stratigraphic surfaces. Location*
428 *map shows the studied area in the Niger Delta.*

429

430 Pore pressure was measured using the RFT method (repeat formation tester) in different wells (Ek-1,
431 Nk-1 and Ik 1, 2, 3, 4 and 5) of the studied area in several reservoir layers. These pressure data were
432 obtained at depths between 1420 and 4590 m (Figure 6.a). Pore pressure shows deviation from the
433 hydrostatic pressure profile at depths greater than 2400 m, indicating an overpressure in these layers.
434 The overpressure can reach up to 500 bar (50 MPa) in the deepest measurements. Two different
435 overpressure regimes seem to be measured, at depths shallower or deeper than 3500 m. Between 2400
436 and 3500 m deep, measured pore pressures correspond to equivalent densities of 1300 to 1500 kg.m^{-3} ,
437 while below 3500 m the pore equivalent density is about 2100 kg.m^{-3} . These two different
438 overpressure regimes can indicate different mechanisms of overpressure generation.

439 Temperature measurements according to depth were also performed in the different wells (Figure 6.b).
 440 The measured temperatures align with a linear geothermal gradient of $30^{\circ}\text{C}.\text{km}^{-1}$, typical of a passive
 441 margin context. Temperature and depth of the shale layers indicate the petroleum window is reached at
 442 the top of the overpressure zone.



443
 444 Figure 6. Measured (a) pore pressure and (b) temperature profiles in wells of the Niger Delta studied area. The pressure
 445 regimes corresponding to equivalent densities (ρ_{eq}) of 1300, 1500 and 2100 $\text{kg}.\text{m}^{-3}$ are also shown.

446
 447 **3.3. Backstripping and sedimentation model**
 448 The sedimentation model aims at determining the successive layers of the sedimentary pile, evaluating
 449 the thickness of these sediments at the deposition time and estimating the sedimentation rate and its
 450 variation over time. With this aim, it is first necessary to uncompact the current sediments to obtain
 451 the thickness of the sediments at the deposition time. The backstripping approach proposed by Sclater
 452 and Christie (1980) for normally compacted sediments of different lithologies was used.
 453 From the geological log and the recorded changes in lithology and rock properties, 45 successive
 454 lithological layers were identified in the sedimentary pile, from the seabed to the foot of Nk-1 well
 455 (Supplementary material B). Over this 4640 m-thickness, the level description in the overpressured
 456 zone (from 2400 m deep) was refined and 39 layers 7 to 407 m thick were defined. On the contrary,
 457 the upper 1040 m of the sand Benin Fm were defined as one single lithological layer. For each
 458 identified layer, the footwall and the roof depth of each lithological layer and the porosity or the
 459 apparent density were reported. Three lithology types were considered and assigned to each identified

460 layer: ‘shale’ for the clay rich layers; ‘shaly-sandstone’ for closely grouped alternations of claystone
461 and sandstone layers; and ‘sandstone’ for the sandstone and sand layers.

462 The second step is the application of the backstripping model in itself, which consists in solving the
463 following equation for each lithological layer:

$$z'_2 - z'_1 = z_2 - z_1 - \frac{n_0}{c} (e^{-c z_1} - e^{-c z_2}) + \frac{n_0}{c} (e^{-c z'_1} - e^{-c z'_2}) \quad \text{eq. 19}$$

464 z_1 and z_2 are the present day roof and footwall depths (m) of the considered lithological layer, z'_1 and
465 z'_2 are the depths at the time of deposit ($z'_1 = 0$ m) assuming that the deposit of the entire lithological
466 layer is instantaneous. n_0 is the surface porosity which depends on the lithology (0.49 for ‘sandstone’
467 facies, 0.56 for ‘shaly-sandstone’ facies and 0.63 for ‘shale’ facies; Sclater and Christie (1980)). c is a
468 compaction index dependent on the lithology ($2.7 \cdot 10^{-4} \text{ m}^{-1}$ for ‘sandstone’ facies, $3.9 \cdot 10^{-4} \text{ m}^{-1}$ for
469 ‘shaly-sandstone’ facies and $5.1 \cdot 10^{-4} \text{ m}^{-1}$ for ‘shale’ facies).

470 Finally, the sedimentation rate was calculated (Table 4) using the sediment thickness at the deposit
471 time and the dating of remarkable sedimentary surfaces. Based on the evolution of the sedimentation
472 rate over time, a period from 7.3 to 6 My can be identified when sedimentation was intense with a rate
473 of almost 3000 m.My^{-1} . After 5.2 My, the sedimentation rate decreased down to about 125 m.My^{-1} .

474 *Table 4. Sedimentation rate for the studied area of the Niger Delta determined for different time periods.*

Period	Sedimentation rate (m.My^{-1})
9.86 to 7.30 My	508.1
7.30 to 6.00 My	2868.3
6.00 to 5.20 My	429.5
5.20 My to present	124.6

475

476 **3.4. Overpressure calculations for the Niger Delta case**

477 **3.4.1. Calculation scenario**

478 The thermo-hydro-mechanical model coupled to chemical processes (SURP) previously presented was
479 used to calculate the pore pressure evolution along the sedimentary pile of the studied area of the
480 Niger Delta during its burial. The considered geometry is a 1D column from the seabed to the footwall

481 of the Agbada Fm. Seismic profiles indicate that the Akata Fm is located some hundreds of meters
482 below the well foots. To deal with the boundary condition between the Agbada and Akata formations
483 and without information about the inflow over time from the Akata Fm, it was decided that 500 m of
484 ‘shale’ lithology at the foot of the modelled sedimentary pile would be included to consider the water
485 inflow from the overpressured Akata Fm. A no flow Neumann boundary condition was considered at
486 the base of these additional 500 m of shale. Additional causes of overpressure proposed for the Niger
487 Delta, such as lateral tectonic compression due to shale diapirism, were not taken into account in the
488 model. As the upper hydraulic boundary condition, hydrostatic pressure was imposed down to the
489 aquifer overlying the overpressured zone (layer shsd11, in Supplementary material B), meaning that
490 the lateral groundwater circulations occurring close to the ground surface did not require to be
491 considered.

492 The principle of the reactive model rests on the hypothesis of seawater as the initial sediment pore
493 water and an initial mineralogical assemblage that evolves as a function of temperature increase with
494 burial. In the absence of a detailed mineralogical description of the shale layers, a fictive but realistic
495 mineralogical assemblage was considered. The ‘sandstone’ facies was assumed to be composed only
496 of quartz. In the ‘shale’ and ‘shaly-sandstone’ lithologies, the primary mineralogical assemblage was
497 composed of montmorillonite, microcline, quartz, calcite, siderite, dolomite, pyrite and goethite. The
498 dehydration of montmorillonite took place in accordance with the thermodynamic dehydration model
499 introduced in the SURP code. Illite and kaolinite were allowed to precipitate during the simulation
500 (Supplementary material C). Water/rock reactions were controlled by thermodynamic equilibrium and
501 not by kinetics, impeding the coexistence of some aluminosilicate minerals. The assumption of a local
502 equilibrium between pore water and the surrounding reacting minerals relies mainly on the fact that
503 the interaction time was long enough to establish equilibrium conditions.

504 The simulation was run for a duration of 9.5 My, corresponding to the deposition time of the sediment
505 column drilled in the Ek-1 and Nk-1 wells. At each time step and depending on the sedimentation rate,
506 a thickness of sediment deposit and the underlying sediments already deposited are buried accordingly
507 because of the compaction model.

508

509 3.4.2. Overpressure calculation results

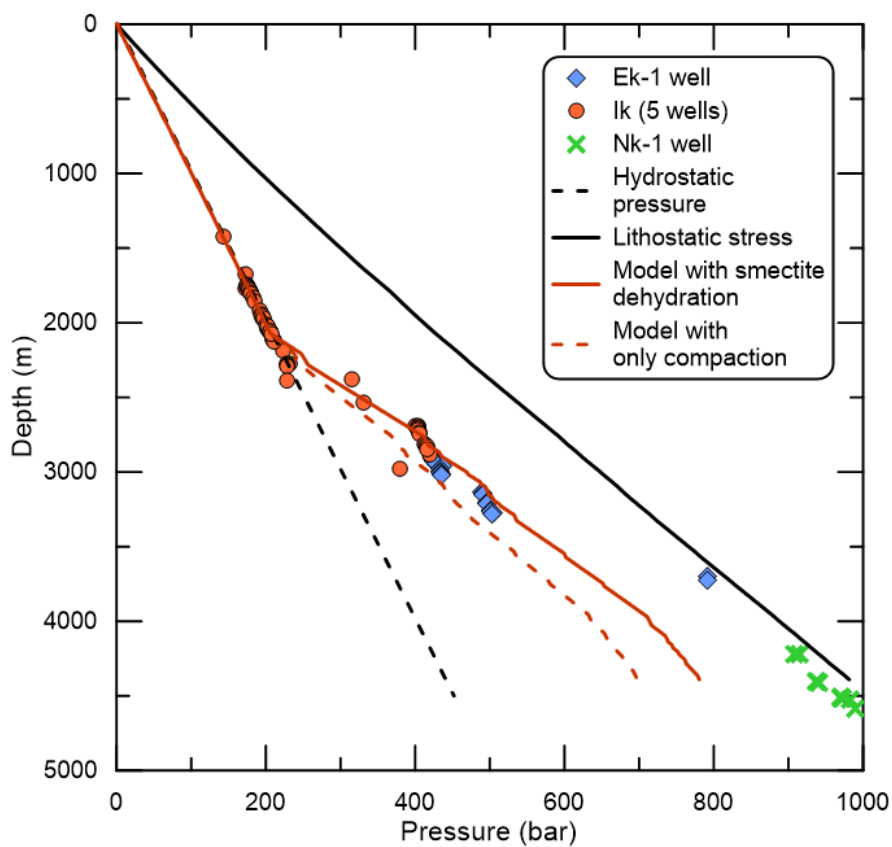
510 The calculated pore pressure at present day in the Niger Delta case was approximately 450 bar at 3000
511 m deep (Figure 7), corresponding to an overpressure of 150 bar at the depth of the main reservoirs. At
512 3000 m deep, good agreement was achieved between the modelled and measured fluid pressures. Two
513 pressure regimes in the overpressured zone were simulated for the profile (between 2750 and 3500 m
514 and below 4000 m), as was observed on the measured pressure profile. Nevertheless, the simulations
515 did not reproduce the deepest (< 4000 m) measured pressures. Indeed, the model does not take into
516 account the influence of the deep Akata shale on overpressures and this influence seems to explain the
517 remaining 100 to 200 bar required to match the present day pressure profile.

518 According to the calculations, smectite dehydration was inducing an excess pressure of about 50 bar
519 on the present day pressure profile at 3000 m deep compared to the simulation accounting only for
520 compaction and thermal effects (Figure 7). The release of water due to smectite dehydration and
521 illitisation can explain a third of the overpressure. A simulation performed accounting for smectite
522 dehydration but without smectite illitisation gave a pressure 5 bar lower than the pressure calculated
523 considering both smectite dehydration and illitisation (in addition to the thermo-mechanical
524 phenomena) at 3000 m deep, and 10 bar lower at the bottom of the modelled sedimentary column.
525 Smectite dehydration thus appears as the main source of water released by smectite. The initial amount
526 of smectite in the sediment also has an influence on the generated overpressure. For example, by
527 dividing the amount of Na-montmorillonite by two (15 %_{vol} for ‘shale’ facies and 7.5%_{vol} for ‘shaly-
528 sandstone’ facies), the calculated overpressure at the present day is 20 bar higher than without the
529 release of water by smectite at 3000 m deep, corresponding to 10 to 15 % of the total overpressure.

530 Figure 8 shows the evolution of the calculated overpressure over time since the beginning of the
531 sediment deposition and as a function of depth. The period with a high sedimentation rate is well
532 identified in this figure where major burial and sediment accumulation was simulated. It resulted in a
533 build-up of the overpressure, which reached values of 500 bar at the bottom of the sedimentary pile
534 and 400 bar at 3000 m deep during this high sedimentation rate period. This pressure build-up is
535 related to the compaction disequilibrium that occurred during this period with the fluids stressed
536 within the porosity, the increase of fluid volume with temperature (aquathermal expansion) and the

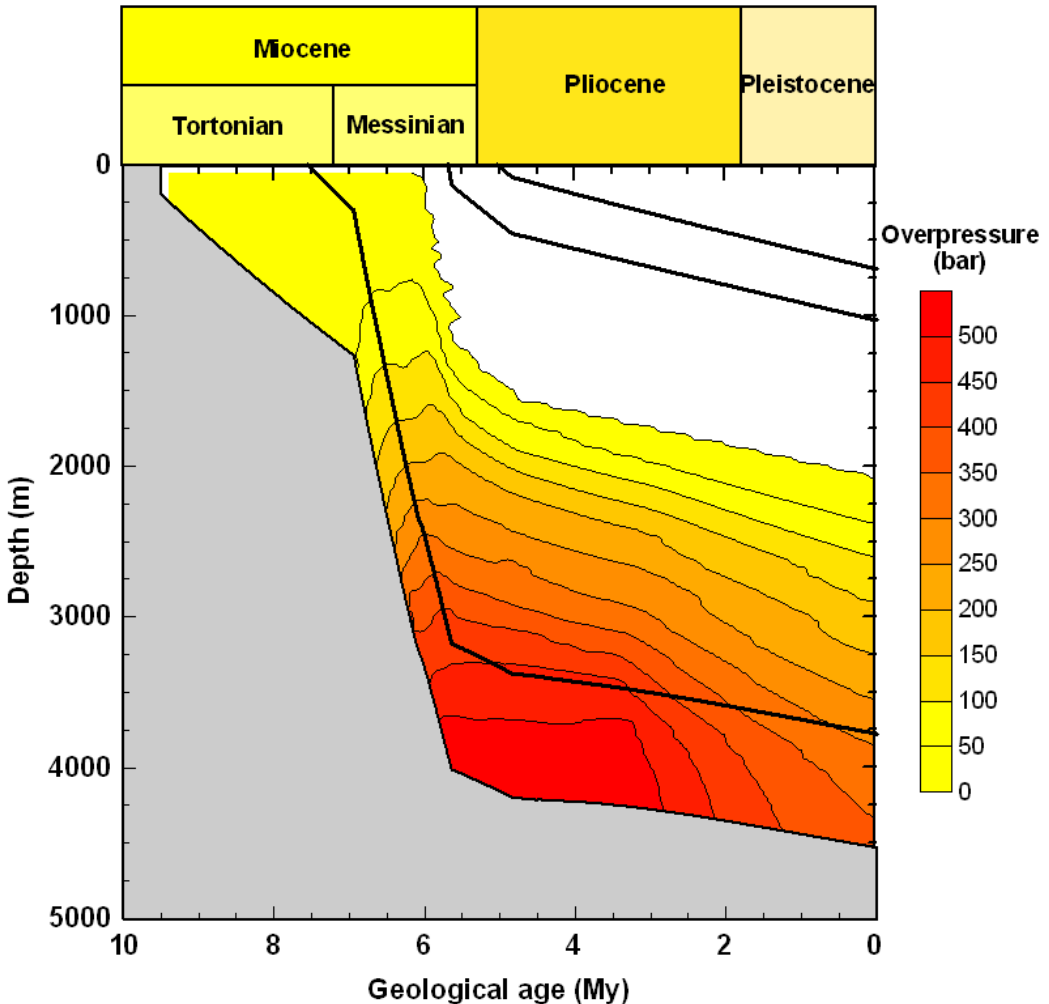
537 release of water from clay minerals that was more efficient with the rapid increases in temperature and
538 pressure. When only compaction and thermal effects were considered, the maximal overpressure
539 reached within this period was 350 bar at 3000 m and 500 bar at the bottom of the modelled column.
540 The overpressure was then simulated to dissipate after the Pliocene, when the sedimentation rate
541 noticeably decreased. Compaction and water release by smectite were less efficient during this final
542 period, allowing the pressure to decrease depending on the hydraulic parameters acquired during
543 burial.

544



545

546 *Figure 7. Present day modelled and observed pore pressure profiles in the Niger Delta area considered for SURP*
547 *application. By comparing the two models which may or may not account for the chemical processes, the effect of the release*
548 *of water by smectite dehydration and illitisation on the abnormal fluid pressure can be evaluated.*



549

550 *Figure 8. Simulated overpressure evolution as a function of geological age and depth in the Niger Delta. The grey area*
 551 *corresponds to a zone outside of the model. The simulation accounts for the clay dehydration and smectite-to-illite*
 552 *transformation processes.*

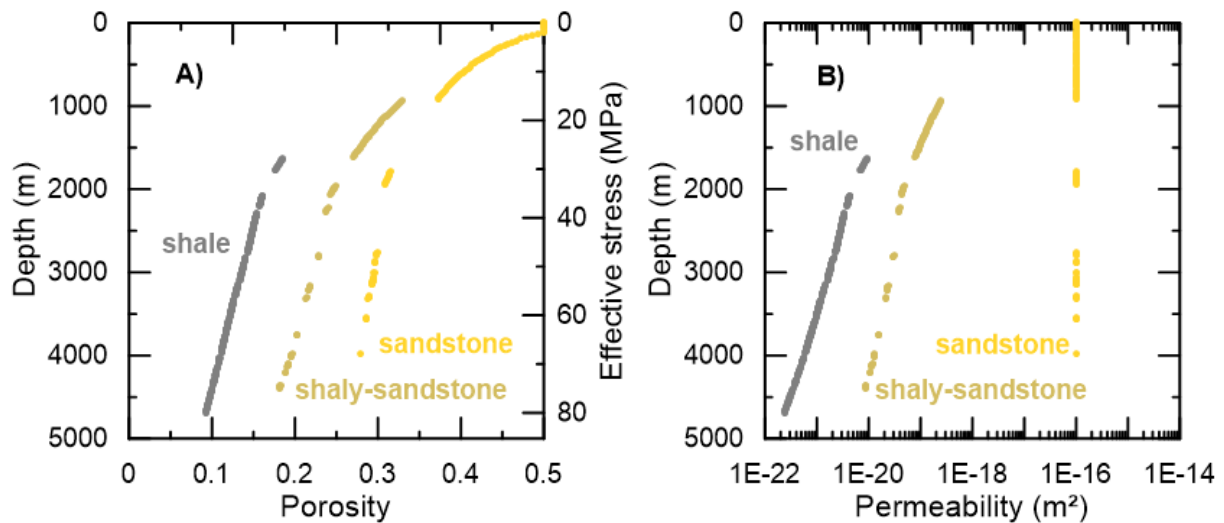
553

554 3.4.3. Compaction model results

555 After 9.5 My of simulation, the model gave a sediment thickness of 4428 m to be compared to the
 556 4640 m of the well log. This sediment thickness was achieved after the initial backstripping
 557 calculation followed by the forward modelling of the deposition and burial of the sediments for
 558 overpressure evaluation. The main difference in thickness between the model and the field resided in
 559 the superior sandstone layer that was not uncompacted during backstripping and was modelled at a
 560 thickness of 956 m compared to the well thickness of 1040 m. Moreover, compaction was slightly
 561 overestimated for ‘shale’ facies ($\approx 5\%$) and underestimated for ‘sandstone’ facies ($\approx 2\%$).
 562 The porosity decreased because of compaction for each lithology (Figure 9.a), with porosities lower
 563 than 15% below 3000 m for the ‘shale’ facies at present day. Hydraulic permeability (Figure 9.b) and

564 other porosity-dependent hydro-mechanical parameters evolved as the porosity decreased. The
 565 permeability reached values of about 10^{-21} m² for the ‘shale’ lithology at depth, forming an efficient
 566 caprock to limit the dissipation of the overpressure built up during the maximal burial period, so that
 567 the overpressure is still monitored at present day. Permeability for ‘shaly-sandstone’ facies was
 568 simulated between 10^{-19} and 10^{-20} m² and permeability for ‘sandstone’ remained constant at 10^{-16} m².

569



570

571 *Figure 9. Simulated present day (a) porosity and (b) permeability profiles. The 3 lithological facies used in the model are*
 572 *distinguished by their colour, showing the difference in compaction trends for each facies.*

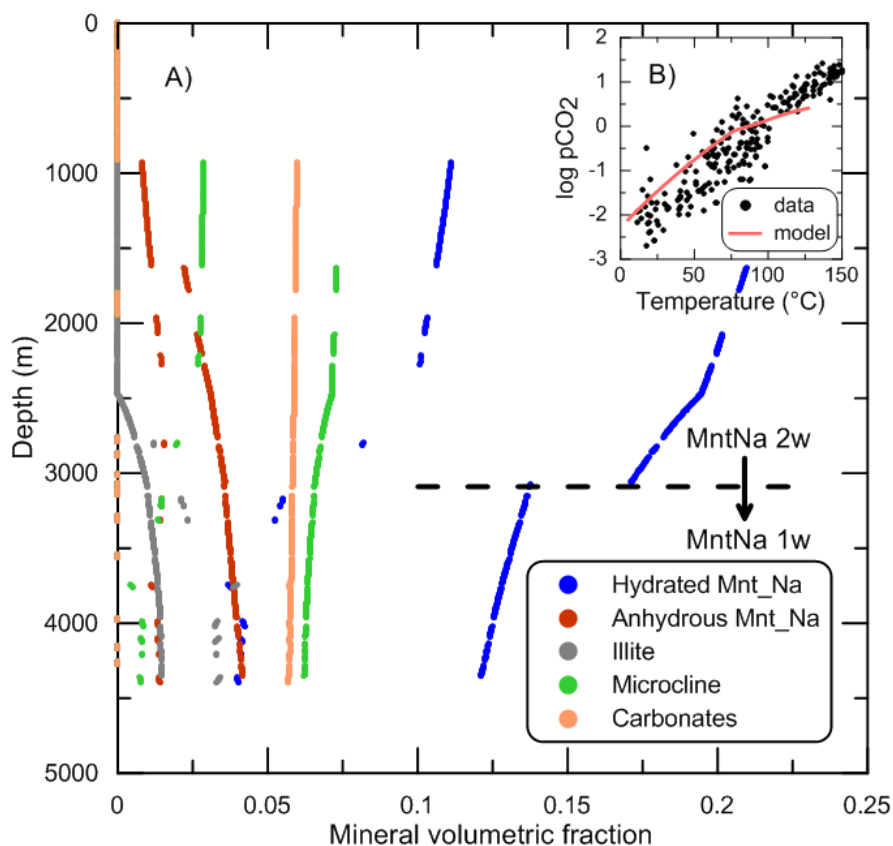
573

574 3.4.4. Mineralogical evolution results

575 The mineralogical evolution can be inferred by the present day mineralogical profile (Figure 10), at
 576 the end of the simulation. The ‘shale’ and ‘shaly-sandstone’ facies are identified in the profile by the
 577 differences in mineral content. Mineralogical composition evolves with depth because temperature is
 578 the main reactivity factor of control. Hydrated Na-montmorillonite content is observed to diminish
 579 with depth while anhydrous Na-montmorillonite content increases, revealing the dehydration of Na-
 580 montmorillonite. The transition from hydrated Na-montmorillonite with two layers of water to one
 581 layer of water is located at about 3070 m (96 °C and 485 bar) and corresponds to a sudden release of
 582 water. The transition from three layers of water to two layers is not observed on the present day profile
 583 because this transition occurred at about 850 m (30°C), at a depth where the ‘sandstone’ lithology is
 584 currently found. Hydrated montmorillonite content also concomitantly decreases at the depth where

illite forms (about 2500 m). Dissolution of microcline also accompanied this illitisation on the profile, acting as a source of K^+ that stabilizes illite. The modelled mineralogical evolution is thus consistent with the expected smectite-to-illite reactive pathway and smectite dehydration process. The evolution of the calculated CO_2 partial pressure with increasing temperature (Figure 10.B) is in line with the pCO_2 usually measured in sedimentary basins (Coudrain-Ribstein et al., 1998). Since the pCO_2 is calculated from an equilibrium between the different involved minerals and the pore water for evolving temperature and pressure conditions, the agreement between calculated and measured pCO_2 is an another indication of the consistence of the mineralogical assemblage selection.

593



594

Figure 10. A) Simulated present day mineralogical profile. Hydrated Mnt_Na: 3w, 2w or 1w Na-montmorillonite; Anhydrous Mnt_Na: anhydrous Na-Montmorillonite; Carbonates: sum of calcite, dolomite and siderite. B) Comparison of calculated pCO_2 with pCO_2 data from sedimentary formations (Coudrain-Ribstein et al., 1998). With the exception of the Mnt_Na 2w to Mnt_Na 1w hydrated smectite transition, the discontinuities in mineral content that are seen in the profile are linked to the distribution of lithological facies with depth.

600

601 4. Discussion

602 A thermo-hydro-mechanical model coupled with an advanced thermodynamic model for smectite
603 dehydration has been developed to calculate overpressures during the burial of a sedimentary pile.

604 Named SURP, this overpressure calculation code accounts for mechanical compaction, thermal effects
605 and water release by smectite. Hence, the effect of pressure and temperature on the smectite
606 dehydration process can be taken into account and the water released is considered in the pressure
607 calculation. This coupling clearly goes beyond the previous models that considered smectite
608 dehydration through an approximated evaluation of a source term in the overpressure calculation
609 (Audet, 1995; Wangen, 2001) or considered smectite dehydration properly but without a feedback on
610 pressure (Colten-Bradley, 1987; Meiller, 2013).

611 The SURP code was applied to the case study of the Niger Delta, formed of thick shale layers.
612 Depending on the clay content, smectite dehydration was simulated to be the cause of 10 to 30 % of
613 the present day overpressure in the main reservoirs, in addition to the compaction disequilibrium. The
614 overpressure built-up during the Messinian is still high (about 200 bar at 3000 m deep) despite its
615 dissipation. Water release by illitisation of smectite has much less influence on the pressure profile
616 than smectite dehydration.

617 Although dependent on the smectite content in the sedimentary pile, the geological scenario and the
618 hydraulic conditions and parameters, the calculated contribution of smectite dehydration to
619 overpressure is in the range of previously estimated contributions. Audet (1995) calculated that
620 dehydration can increase overpressuring by about 30 % provided that the sediments are relatively
621 impermeable and that sufficient water is released. Also in a theoretical scenario, Wangen (2001)
622 calculated a contribution of smectite dehydration in the same range, of about $\frac{1}{4}$ to $\frac{1}{3}$ of the
623 overpressure. The examples of quantification of the contribution of smectite dehydration to
624 overpressures are few in the literature since the release of water is often considered as only one
625 contributor amongst other unloading processes that decrease the effective stress without modifying the
626 porosity. In the North Sea Viking Graben (Nordgård Bolås et al., 2004) and Central Graben (Kooi,
627 1997), smectite dehydration is discussed as a potential additional overpressuring mechanism as
628 compaction disequilibrium alone is not sufficient to explain the measured overpressure, and other
629 possible mechanisms were ruled out. In the Gulf of Mexico, offshore Louisiana, Gordon and Flemings
630 (1998) simulated that, depending on the elastic or inelastic compaction model considered, clay
631 dehydration can provide up to 20 % of the overpressure. Clay dehydration is also discussed in the Gulf

632 of Mexico as a possible source of overpressure by Bruce (1984) and Shaw and Primmer (1989), based
633 on the observation that the onset of the overpressure coincides with the smectite-to-illite
634 transformation. In the Western Foothills of Taiwan, Tanikawa et al. (2008) performed overpressure
635 calculations suggesting that clay dehydration is a secondary mechanism generating overpressures,
636 complementary to compaction disequilibrium and more significant than hydrocarbon generation. In
637 the Taiwan case, it is estimated that at the maximum pressure build-up, clay dehydration can double
638 the calculated overpressure compared to cases in which only compaction and thermal expansion are
639 taken into account. Overpressure nevertheless dissipated then and a basal fluid flux was necessary to
640 explain the present day pressure profile.

641 Clay dehydration is often ruled out as a mechanism contributing to overpressure because the volume
642 increase due to the water produced by smectite dehydration was estimated at only 1.4 % below a depth
643 of 1 km, which is the depth at which overpressures are observed to develop (Swarbrick and Osborne,
644 1998). Our results are at the opposite: when clay dehydration is integrated in forward modelling of
645 overpressure, the different examples, including ours, suggest that the release of water by smectite
646 dehydration or by illitisation can contribute to the pressure profile as an important additional
647 contributor to compaction disequilibrium.

648 Although able to consider each process that can contribute to the overpressure build-up and dissipation
649 calculations individually, the forward modelling approach we considered presents limitations inherent
650 to every hydraulic and water/rock interaction model. The two key factors in a hydraulic model are the
651 boundary conditions and their evolution over time, and the hydraulic conductivity and its dependence
652 on compaction and porosity reduction (Person et al., 1996; Bjørlykke et al., 2010). The hydraulic
653 boundary condition at the base of the sedimentary pile is generally unknown and a simple and
654 idealized boundary condition is often considered. A no flow basal boundary condition is a convenient
655 approach but is evidently complicated to verify. In the case of the Niger Delta, we had no information
656 about an inflow at 5000 m deep, at the bottom of the sedimentary pile of our model. Seismic data
657 indicated an apparent density in line with the deepest pressure measurements. The hydraulic and
658 hydro-mechanical parameters used in the simulation have a high influence on the flow and pressure
659 regime in the modelled sedimentary pile. In our study, we used porosity-dependent empirical

660 relationships to determine these parameters, calibrated on various sets of experimental data
661 (Supplementary material A). The scattering of the data around the empirical relationships illustrates
662 the variability of these parameters. When data from the studied site are available, the empirical
663 relationships can be calibrated on these data. However, data scattering around the law may be
664 unavoidable, which may affect the robustness of the law.

665 Limitations of the water/rock interaction model rely on the fact that it is necessary to know the pore
666 water composition and its evolution, and that mineralogical and petrographical data are necessary for
667 good constraining of the interaction model (Person et al., 1996). For instance, the depths of the
668 smectite dehydration reactions and the smectite-to-illite transformation may vary significantly
669 according to the chemical composition of the clay phases or the variation of the thermodynamic
670 parameters within their error margins. Based on this knowledge and on the reasonable assumptions
671 that seawater was trapped in the sediment porosity and that the initial mineralogical assemblage
672 corresponded to a clay-rich sediment, our model has been able to simulate the expected illitisation of
673 smectite, accompanied by microcline dissolution. Reactive transport models have already been applied
674 to diagenesis modelling (e.g. Le Gallo et al., 1998), giving valuable simulations of mineral evolution
675 in reservoirs.

676

677 **5. Conclusion**

678 In this study, we developed the first overpressure calculation code including a thermodynamic
679 description of clay dehydration. We draw upon recent advances in clay thermodynamics and in
680 numerical modelling of solid solutions to precisely calculate the quantity of water that can be expelled
681 within the porosity of clay formations during smectite dehydration and illitisation processes. Hence,
682 the SURP code considers water flow, compaction, temperature increase and smectite dehydration and
683 illitisation, with a reciprocal effect, during the burial of a sedimentary pile.

684 The application of the SURP code to the Niger Delta case study evidenced that 10 to 30 % of the
685 present day overpressure in the main reservoirs can be explained by smectite dehydration. Up to now,
686 relatively few cases of overpressures generated by smectite dehydration have been reported and this
687 mechanism is often not considered because of the lack of a tool able to calculate its effect. With a code

688 such as SURP, it is possible to evaluate the influence of smectite dehydration on overpressure build-up
689 in passive margins, but also in compressive domains.

690 One of the future prospects of this work should be the introduction of this type of calculation in 2D or
691 3D basin modelling in order to better constrain boundary conditions and investigate how the water
692 production by clay formations can contribute to the general fluid flow in the basin. Another prospect
693 should be the improvement of the capabilities of the SURP code in simulating coupled mineralogical
694 and hydro-mechanical evolution as a diagenesis code that can differentiate the porosity evolution due
695 to mechanical compaction and diagenesis.

696

697 **Acknowledgments**

698 This work was funded by TOTAL S.A. The authors are grateful to two anonymous reviewers for their
699 helpful comments and to Friedemann Baur associate Editor for handling the manuscript.

700

701 **References**

- 702 Altaner, S.P., 1989. Calculation of K diffusional rates in bentonite beds. *Geochimica et Cosmochimica
703 Acta* 53, 923–931.
- 704 Altaner, S.P., Ylagan, R.F., 1997. Comparison of structural models of mixed-layer illite/smectite and
705 reaction mechanisms of smectite illitization. *Clays and Clay Minerals* 45, 517–533.
- 706 Audet, D.M., 1995. Mathematical modelling of gravitational compaction and clay dehydration in thick
707 sediment layers. *Geophysical Journal International* 122, 283–298.
- 708 Bjørlykke, K., Jahren, J., Aagaard, P., Fisher, Q., 2010. Role of effective permeability distribution in
709 estimating overpressure using basin modelling. *Marine and Petroleum Geology* 27, 1684–
710 1691.
- 711 Blanc, P., Lassin, A., Piantone, P., Azaroual, M., Jacquemet, N., Fabbri, A., Gaucher, E.C., 2012.
712 Thermoddem: A geochemical database focused on low temperature water/rock interactions
713 and waste materials. *Applied Geochemistry* 27, 2107–2116.
- 714 Blanc, P., Vieillard, P., Gailhanou, H., Gaboreau, S., Gaucher, E., Fialips, C. I., Giffaut, E., 2015. A
715 generalized model for predicting the thermodynamic properties of clay minerals. *American
716 Journal of Science* 315, 734–780.
- 717 Braide, S.P., Huff, W.D., 1986. Clay mineral variation in Tertiary sediments from the eastern flank of
718 the Niger Delta. *Clay Minerals* 21, 211–224.
- 719 Bruce, C.H., 1984. Smectite dehydration; its relation to structural development and hydrocarbon
720 accumulation in northern Gulf of Mexico basin. *AAPG Bulletin* 68, 673–683.
- 721 Burland, J.B., 1990. On the compressibility and shear strength of natural clays. *Géotechnique* 40, 329–
722 378.
- 723 Burrus, J., 1998. Overpressure models for clastic rocks, their relation to hydrocarbon expulsion: a
724 critical reevaluation, in: Law, B.E., Ulmishek, G.F., Slavin, V.I. (Eds.), *AbnormalPressures
725 Hydrocarbon Environments*, AAPGMemoir. AAPG, pp. 35–64.
- 726 Burst, J.F., 1969. Diagenesis of Gulf Coast clayey sediments and its possible relation to petroleum
727 migration. *AAPG Bulletin* 53, 73–93.
- 728 Caillet, G., Batiot, S., 2003. 2D modelling of hydrocarbon migration along and across growth faults:
729 an example from Nigeria. *Petroleum Geoscience* 9, 113–124.

- 730 Charlton, S.R., Parkhurst, D.L., 2011. Modules based on the geochemical model PHREEQC for use in
731 scripting and programming languages. *Computers & Geosciences* 37, 1653–1663.
- 732 Chukwu, G.A., 1991. The Niger Delta complex basin: stratigraphy, structure and hydrocarbon
733 potential. *Journal of Petroleum Geology* 14, 211–220.
- 734 Cobbold, P.R., Clarke, B.J., Loseth, H., 2009. Structural consequences of fluid overpressure and
735 seepage forces in the outer thrust belt of the Niger Delta. *Petroleum Geosciences* 15, 3–15.
- 736 Colten-Bradley, V.A., 1987. Role of pressure in smectite dehydration; effects on geopressure and
737 smectite-to-illite transformation. *AAPG Bulletin* 71, 1414–1427.
- 738 Coudrain-Ribstein, A., Gouze, P., Marsily, G. de, 1998. Temperature–carbon dioxide partial pressure
739 trends in confined aquifers. *Chemical Geology* 145, 73–89.
- 740 Cuadros, J., 2006. Modeling of smectite illitization in burial diagenesis environments. *Geochimica et
741 Cosmochimica Acta* 70, 4181–4195.
- 742 De Marsily, G., 1986. Quantitative Hydrogeology. Academic Press.
- 743 Dubacq, B., Vidal, O., De Andrade, V., 2010. Dehydration of dioctahedral aluminous phyllosilicates:
744 thermodynamic modelling and implications for thermobarometric estimates. *Contributions to
745 Mineralogy and Petrology* 159, 159–174.
- 746 Ferrage, E., Lanson, B., Sakharov, B.A., Drits, V.A., 2005. Investigation of smectite hydration
747 properties by modeling experimental X-ray diffraction patterns: Part I. Montmorillonite
748 hydration properties. *American Mineralogist* 90, 1358–1374.
- 749 Gordon, D.S., Flemings, P.B., 1998. Generation of overpressure and compaction-driven fluid flow in a
750 Plio-Pleistocene growth-faulted basin, Eugene Island 330, offshore Louisiana. *Basin Research*
751 10, 177–196.
- 752 Ingebritsen, S., Sanford, W., Neuzil, C., 2006. Groundwater in geologic processes. Cambridge
753 University Press.
- 754 Inoue, A., Kohyama, N., Watanabe, T., 1987. Chemical and morphological evidence for the
755 conversion of smectite to illite. *Clays and Clay Minerals* 35, 111–120.
- 756 Jubril, M.A., Shaw, H.F., Fallick, A.E., 1998. Stable isotope and geochemical evidence of formation
757 pore fluid evolution during diagenesis of Tertiary sandstones and mudrocks of the Niger Delta.
758 *Journal of African Earth Science* 27, 417–435.
- 759 Kooi, H., 1997. Insufficiency of compaction disequilibrium as the sole cause of high pore fluid
760 pressures in pre-Cenozoic sediments. *Basin Research* 9, 227–241.
- 761 Lambe, T.W., Whitman, R.V., 1979. Soil mechanics, Series in soil engineering. Wiley.
- 762 Lanson, B., Sakharov, B.A., Claret, F., Drits, V.A., 2009. Diagenetic smectite-to-illite transition in
763 clay-rich sediments: A reappraisal of X-ray diffraction results using the multi-specimen
764 method. *American Journal of Science* 309, 476–516.
- 765 Le Gallo, Y., Bildstein, O., Brosse, E., 1998. Coupled reaction-flow modeling of diagenetic changes in
766 reservoir permeability, porosity and mineral compositions. *Journal of Hydrology* 209, 366–
767 388.
- 768 Meiller, C., 2013. Etude cristallochimique de solutions solides de minéraux argileux. Impact de la
769 déshydratation des smectites sur les surpressions dans les bassins sédimentaires.
- 770 Meunier, A., Velde, B., 1989. Solid solution in I/S mixed-layer minerals and illite. *American
771 Mineralogist* 74, 1106–1112.
- 772 Neuzil, C.E., 1995. Abnormal pressures as hydrodynamic phenomena. *American Journal of Science*
773 295, 742–786.
- 774 Nordgård Bolås, H.M., Hermanrud, C., Teige, G.M., 2004. Origin of overpressures in shales:
775 Constraints from basin modeling. *AAPG bulletin* 88, 193–211.
- 776 Nwozor, K.K., Omudu, M.L., Ozumba, B.M., Egbuachor, C.J., Onwuemesi, A.G., Anike, O.L., 2013.
777 Quantitative evidence of secondary mechanisms of overpressure generation: insights from
778 parts of onshore Niger Delta, Nigeria. *Petroleum Technology Development Journal* 3, 64–83.
- 779 Nygård, R., Gutierrez, M., Gautam, R., Høeg, K., 2004. Compaction behavior of argillaceous
780 sediments as function of diagenesis. *Marine and Petroleum Geology* 21, 349–362.
- 781 Oboh, F.E., 1992. Middle Miocene palaeoenvironments of the Niger Delta. *Palaeogeography,
782 Palaeoclimatology, Palaeoecology* 92, 55–84.

- 783 Odigi, M.I., 1986. Mineralogical and geochemical studies of Tertiary sediments from the eastern Niger
784 Delta and their relationship to petroleum occurrence. *Journal of Petroleum Geology* 10, 101–
785 114.
- 786 Opara, A., 2011. Estimation of multiple sources of overpressures using vertical effective stress
787 approach: case study of the Niger Delta, Nigeria. *Petroleum & Coal* 53.
- 788 Owolabi, O.O., Okpobiri, G.A., Obomanu, I.A., 1990. Prediction of abnormal pressure in the Niger
789 Delta Basin using well logs. *SPE 021575*, 1–15.
- 790 Parkhurst, D.L., Appelo, C.A.J., 2013. Description of input and examples for PHREEQC Version 3—a
791 computer program for speciation, batch-reaction, one-dimensional transport, and inverse
792 geochemical calculations. U.S. Geological Survey.
- 793 Perry, E.A., Hower, J., 1970. Burial diagenesis in Gulf Coast pelitic sediments. *Clays and Clay
794 Minerals* 18, 165–177.
- 795 Person, M., Raffensperger, J.P., Ge, S., Garven, G., 1996. Basin-scale hydrogeologic modeling.
796 *Reviews of Geophysics* 34, 61–87.
- 797 Pytte, A.M., Reynolds, R.C., 1989. The thermal transformation of smectite to illite, in: Naeser, T.H.
798 N.D. McCulloh (Ed.), *The Thermal History of Sedimentary Basins*. Springer, New York, pp.
799 133–140.
- 800 Ransom, B., Helgeson, H.C., 1994. A chemical and thermodynamic model of aluminous dioctahedral
801 2:1 layer clay minerals in diagenetic processes; regular solution representation of interlayer
802 dehydration in smectite. *American Journal of Science* 294, 449–484.
- 803 Saffer, D.M., McKiernan, A.W., 2009. Evaluation of in situ smectite dehydration as a pore water
804 freshening mechanism in the Nankai Trough, offshore southwest Japan. *Geochemistry,
805 Geophysics, Geosystems* 10.
- 806 Slater, J.G., Christie, P.A.F., 1980. Continental stretching: An explanation of the Post-Mid-
807 Cretaceous subsidence of the central North Sea Basin. *Journal of Geophysical Research: Solid
808 Earth* 85, 3711–3739.
- 809 Shaw, H.F., Primmer, T.J., 1989. Diagenesis in shales from a partly overpressured sequence in the
810 Gulf Coast, Texas, USA. *Marine and Petroleum Geology* 6, 121–128.
- 811 Srodon, J., Zeelmaekers, E., Derkowsky, A., 2009. The charge of component layers of illite-smectite in
812 bentonites and the nature of end-member illite. *Clays and Clay Minerals* 57, 649–671.
- 813 Swarbrick, R.E., Osborne, M.J., 1998. Mechanisms that Generate Abnormal Pressures: an Overview,
814 in: Law, B.E., Ulmishek, G.F., Slavin, V.I. (Eds.), *AbnormalPressures Hydrocarbon
815 Environments*, AAPGMemoir. AAPG, pp. 13–34.
- 816 Tanikawa, W., Shimamoto, T., Wey, S., Lin, C., Lai, W., 2008. Stratigraphic variation of transport
817 properties and overpressure development in the Western Foothills, Taiwan. *Journal of
818 Geophysical Research: Solid Earth* 113.
- 819 Tremosa, J., Gonçalvès, J., Matray, J.M., 2012. Natural conditions for more limited osmotic abnormal
820 fluid pressures in sedimentary basins. *Water Resources Research* 48.
- 821 Ugwu, S.A., Nwankwo, C.N., 2014. Integrated approach to geopressure detection in the X-field,
822 Onshore Niger Delta. *Journal of Petroleum Exploration and Production Technology* 4, 215–
823 231.
- 824 Van Der Kamp, G., Gale, J.E., 1983. Theory of earth tide and barometric effects in porous formations
825 with compressible grains. *Water Resources Research* 19, 538–544.
- 826 Velde, B., Brusewitz, A.M., 1986. Compositional variation in component layers in natural
827 illite/smectite. *Clays and Clay Minerals* 34, 651–657.
- 828 Velde, B., Vasseur, G., 1992. Estimation of the diagenetic smectite to illite transformation in time-
829 temperature space. *American Mineralogist* 77, 967–976.
- 830 Vidal, O., Dubacq, B., 2009. Thermodynamic modelling of clay dehydration, stability and
831 compositional evolution with temperature, pressure and H₂O activity. *Geochimica et
832 Cosmochimica Acta* 73, 6544–6564.
- 833 Wangen, M., 2001. A quantitative comparison of some mechanisms generating overpressure in
834 sedimentary basins. *Tectonophysics* 334, 211–234.
- 835 Weaver, C.E., 1959. Possible uses of clay minerals in the search for oil. *Clays and Clay Minerals* 8,
836 214–227.
- 837 Whiteman, A., 1982. Nigeria: its petroleum geology, resources and potential. Graham & Trotman.